Robust Algorithm of Time-domain Distance Protection for Renewable Power Transmission System with Mixed Overhead Lines and Underground Cables

Bin Li, *Fellow*, *IEEE*, Zhongrun Xie, Jiawei He, *Member*, *IEEE*, Mingyu Shao, Haiji Wang, and Zepeng Hu

***Abstract*—Time-domain distance protection shows superior performance for transmission lines integrated with renewable energy sources (RESs). However, in 35-110 kV renewable power transmission systems, the inhomogeneity of the mixed overhead lines (OHLs) and underground cables (UGCs) negatively affects the feasibility of distance protection. This paper proposes a robust algorithm of time-domain distance protection for renewable power transmission system with the mixed OHLs and UGCs. First, based on the time-domain mathematical model, the accuracy and robustness of the conventional algorithm under inhomogeneous line parameters are evaluated. To solve the "0/0" problem caused by weak signals, the singular value decomposition-based least squares method (SVD-LSM) is adopted to avoid calculation outliers and improve the protection reliability. Meanwhile, a weighting method based on Euclidean norm is designed to overcome the problem of computational non-convergence. It also ensures the protection operation speed by using a short time window. In addition, a distance correction method is designed for mixed lines to improve the accuracy of fault location. On the basis, a prototype of the protection device is developed, and extensive hardware-in-the-loop (HIL) tests are performed to verify its feasibility and superiority. In addition, the prototype of the protection device has been applied to actual renewable power transmission systems.**

***Index Terms*—Renewable energy source (RES), transmission line, distance protection, fault location, overhead line (OHL), underground cable (UGC).**

I. Introduction

THE integration of renewable energy sources (RESs) into urban power grids has increased markedly in recent years [1]. Consequently, it is of the utmost importance to guarantee secure and reliable operation of power systems under the integration of large-scale and high-proportional RESs. However, the fault response of RESs has completely different characteristics from synchronous generators, which challenges the adaptability of conventional grid protections [2]-[5].

Line protection in power grids usually adopts single-ended methods (i.e., overcurrent protection and distance protection) and double-ended methods (i. e., current differential protection). For overcurrent protection, the small short-circuit capacity and random output power of RESs lead to difficulties in coordinating the relay settings, which can hardly guarantee the selectivity of the protection [6], [7]. In addition, the frequency of RES short-circuit current may differ from the system frequency, especially for doubly-fed induction generators (DFIGs) [8]-[10]. In this case, the current frequency deviation negatively affects the performance of conventional distance protection based on the Fourier algorithm, which may trip incorrectly during the fault transient stage, as illustrated in Fig. 1. Although current differential protection can be applied to lines with integrated RESs, the small amplitude and phase shift of the fault current on RES station side still affect the sensitivity of the protection [11], [12]. In addition, current differential protection relies on communication channels, and the cost and complexity of engineering implementation limit its application at different voltage levels, especially for 35-110 kV renewable power transmission systems.

At present, for the outgoing lines of RES stations with voltage levels below 110 kV in Tianjin urban grid, China, line protection devices based on the single-ended method are generally installed only on the grid side, but not on the RES station side [13], [14]. When a fault occurs, the RES station is usually tripped off and disconnects from the grid via its own frequency and voltage protection. However, the single-ended method has poor selectivity, even with a time delay of 0.2-0.5 s. For example, an external fault outside the Hanzhuang substation (Ninghe District, Tianjin, China) results in the tripping of eight integrated RES stations distributed on different lines.

Manuscript received: May 22, 2024; revised: October 14, 2024; accepted: March 12, 2025. Date of CrossCheck: March 12, 2025. Date of online publication: May 5, 2025.

This work was supported in part by State Key Laboratory of Technology and Equipment for Defense Against Power System Operational Risks (No. SGTYHT/20-JS-221), the National Natural Science Foundation of China for Distinguished Young Scholars (No. 52025071), and the Natural Science Foundation of Tianjin, China (No. 22JCQNJC01030).

B. Li and Z. Xie (corresponding author) are with State Key Laboratory of Technology and Equipment for Defense Against Power System Operational Risks, Nanjing, China, and they are also with Key Laboratory of Smart Grid of Ministry of Education, Tianjin University, Tianjin, China (e-mail: binli@tju.edu.cn; xiezhongrun@tju.edu.cn).

J. He, M. Shao, and Z. Hu are with Key Laboratory of Smart Grid of Ministry of Education, Tianjin University, Tianjin, China (e-mail: hejiawei1991@tju.edu.cn; mingyu@tju.edu.cn; hzp_cqu@tju.edu.cn).

H. Wang is with Xi'an XIRUI Control Technology Co., Ltd., Xi'an, China (e-mail: wanghaiji@cnxirui.com).

DOI: 10.35833/MPCE.2024.000536

To avoid the frequent tripping of RES stations and ensure the power supply reliability, the delay time of frequency and voltage protection should be further extended. However, this extension brings risks to the system operation stability. Therefore, it is necessary to realize fast and selective single-ended method for 35-110 kV renewable power transmission systems.

To address the aforementioned issues, the time-domain distance protection (corresponds to time-domain algorithm in Fig. 1), which employs differential equations to locate faults, is a viable method for renewable power transmission systems [15]-[22], since it is independent of the frequency characteristics of the fault current. The differential equation method proposed in [15]-[18] employs sampled values of measured voltages and currents to calculate the fault distance, which is independent of the fault resistance. The differential equation method exhibits favorable performance for short-distance and medium-distance transmission lines. In [19], a method considering *R-L* and the Bergeron model is proposed for long-distance transmission lines. To further enhance the accuracy of fault location, the high-order differential equation methods are designed in [20] and [21]. In addition, [22] investigates the location error introduced by the fault resistance and proposes an improved method with advantages in calculation convergence, accuracy of fault location, and overreach prevention capability under resistive faults.

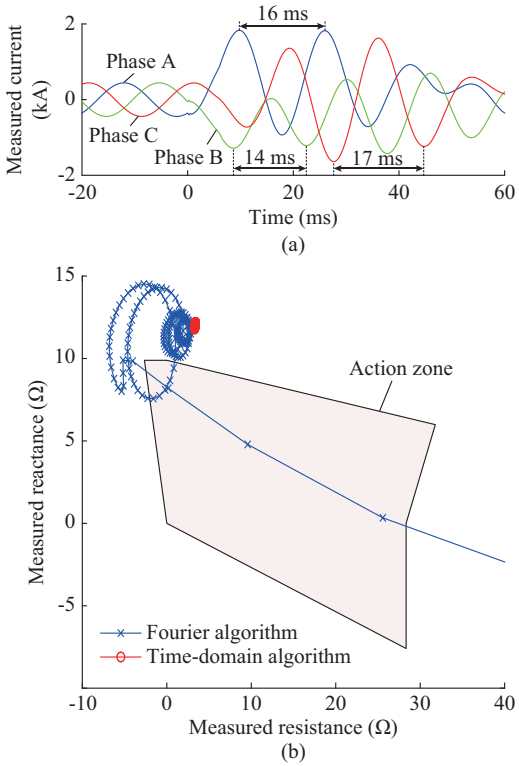

Fig. 1. Performance of distance protection under current frequency deviation (external fault on transmission line with integrated DFIG). (a) Measured current. (b) Measured reactance.

However, the above-mentioned methods are proposed for the single homogeneous line. In the urban power system, the grid connection structure for RES is complex, some feeders consist of multiple overhead line (OHL) and underground cable (UGC) sections. The inhomogeneity of mixed lines (which mean mixed OHL and UGC) introduces obvious calculation errors and can lead to incorrect operation of distance protection, which relies on precise line parameters [23]-[25]. Especially for the time-domain distance protection, the accuracy and reliability of the calculated fault distance results need to be further investigated. Therefore, the engineering application of time-domain distance protection still faces challenges.

The focus of this paper is on the application of time-domain distance protection for 35-110 kV renewable power transmission systems with mixed OHLs and UGCs. It investigates the negative impact of inhomogeneous line parameters on time-domain distance protection, and proposes a robust algorithm to improve the robustness of the protection when applied to complex grid-connected scenarios of RES.

This paper is organized as follows. Section II shows the practical challenges of time-domain distance protection for mixed lines. In Section III, the protection algorithm with high robustness and accuracy is proposed. Section IV shows the experimental test. Section V presents the conclusions.

II. Practical Challenges of Time-domain Distance Protection for Mixed Lines

A. Basic Principle

As illustrated in the renewable power transmission system of Fig. 2(a), when a single-phase-to-ground (SG) fault occurs, the differential equation for the measured voltage and current at node M can be expressed as:

$$u_{M\varphi}=\left[R_1(i_{M\varphi}+3i_{M0}K_{\mathrm{R}})+L_1\frac{\mathrm{d}(i_{M\varphi}+3i_{M0}K_{\mathrm{L}})}{\mathrm{d}t}\right]x+i_{M\varphi}R_{\mathrm{F}}\approx p_{M\varphi}x+3i_{M0}R'_{\mathrm{F}} \tag{1}$$

where the subscripts 0 and 1 denote the variables in zero-sequence and positive-sequence, respectively; the subscript φ denotes the fault phase; x is the fault distance; R_{F} is the fault resistance; $R'_{\mathrm{F}}=R_{\mathrm{F}}/K_{\mathrm{F0}}$, where K_{F0} is the zero-sequence shunt coefficient at the fault location; R and L are the resistance and inductance per unit length of the transmission line, respectively; $u_{M\varphi}$ is the voltage at node M; $i_{M\varphi}$ is the current injected into node M caused by SG fault; $K_{\mathrm{R}}=(R_0-R_1)/(3R_1)$ and $K_{\mathrm{L}}=(L_0-L_1)/(3L_1)$ are the zero-sequence compensation coefficients of the transmission line, respectively; and $p_{M\varphi}$ is the differential function of measured current at node M, i.e., $p_{M\varphi}=R_1(i_{M\varphi}+K_{\mathrm{R}}3i_{M0})+L_1\mathrm{d}(i_{M\varphi}+K_{\mathrm{L}}3i_{M0})/\mathrm{d}t$.

The current injected into the node (fault point) is usually assumed to have the same phase angle as the zero-sequence current measured at the relay location [15]-[18]. Thus, the fault current can be written as $i_{\mathrm{F}\varphi}\approx 3i_{M0}/K_{\mathrm{F0}}$. Thus, $i_{\mathrm{F}\varphi}R_{\mathrm{F}}$ can be replaced with $3i_{M0}R'_{\mathrm{F}}$ in (1) .

A set of differential equations can be constructed by substituting continuously sampled voltages and currents into (1). By employing the least squares method (LSM), the overdetermined system can be solved as:

$$[\hat{x}\quad \hat{R}'_{\mathrm{F}}]^{\mathrm{T}}=(\boldsymbol{I}_{M\varphi}^{\mathrm{T}}\boldsymbol{I}_{M\varphi})^{-1}\boldsymbol{I}_{M\varphi}^{\mathrm{T}}\boldsymbol{U}_{M\varphi} \tag{2}$$

where $\hat{x}$ and $\hat{R}'_{\mathrm{F}}$ are the calculated fault distance and transition resistance through LSM, respectively; and $\boldsymbol{I}_{M\varphi}$ and $\boldsymbol{U}_{M\varphi}$ are the current and voltage matrices formed by the sampled signals, respectively, which can be expressed as:

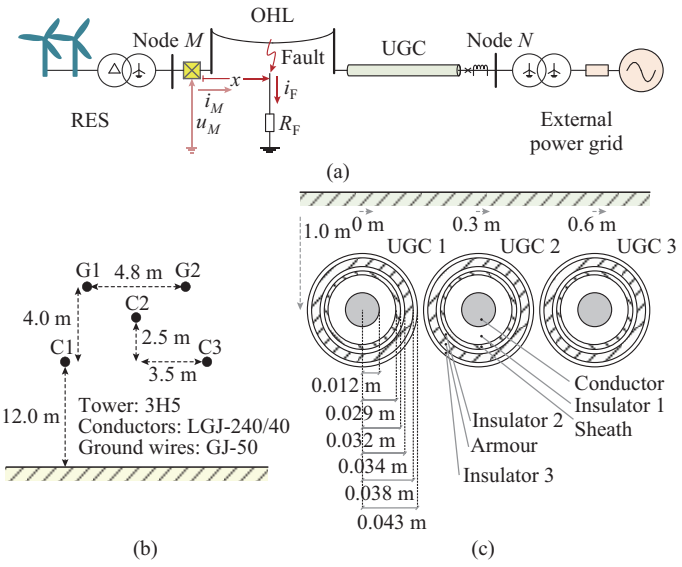

Fig. 2. Schematic diagram of mixed OHLs and UGCs. (a) Renewable power transmission system. (b) Topology of OHL. (c) Topology of UGC.

$$\begin{cases} \boldsymbol{I}_{M\varphi}=\begin{bmatrix} p_{M\varphi}(k_1) & p_{M\varphi}(k_2) & \dots & p_{M\varphi}(k_n) \\ 3i_{M0}(k_1) & 3i_{M0}(k_2) & \dots & 3i_{M0}(k_n) \end{bmatrix}^{\mathrm{T}} \\ \boldsymbol{U}_{M\varphi}=[u_{M\varphi}(k_1) \quad u_{M\varphi}(k_2) \quad \dots \quad u_{M\varphi}(k_n)]^{\mathrm{T}} \end{cases} \tag{3}$$

where k_i is the number of each sampling point, $i=1,2,\dots,n$; n is the number of sampling points per unit time window, i.e., $n=T_{\mathrm{w}}/\Delta t$; T_{w} is the unit time window; Δt is the sampling interval time; and $p_{M\varphi}(k_i)=R_1(i_{M\varphi}(k_i)+K_{\mathrm{R}}3i_{M0}(k_i))+L_1(i_{M\varphi}(k_{i+1})+3i_{M0}(k_{i+1})K_{\mathrm{L}}-i_{M\varphi}(k_{i-1})-K_{\mathrm{L}}3i_{M0}(k_{i-1}))/(2\Delta t)$.

In addition, the differential equation under phase-to-phase faults can be expressed as $u_{M\varphi\varphi}=(R_1 i_{M\varphi\varphi}+L_1\mathrm{d}i_{M\varphi\varphi}/\mathrm{d}t)x+i_{\mathrm{F}\varphi\varphi}R_{\mathrm{F}}\approx(R_1 i_{M\varphi\varphi}+L_1\mathrm{d}i_{M\varphi\varphi}/\mathrm{d}t)x+i_{M\varphi\varphi 2}R'_{\mathrm{F}}$, where $i_{M\varphi\varphi}$ is the current injected into node M caused by phase-to-phase fault; $i_{M\varphi\varphi 2}$ is the negative-sequence current, which is used to replace the current injected into the fault point $i_{\mathrm{F}\varphi\varphi}$ to improve the calculation accuracy [22]. In this case, the simplified differential equation for phase-to-phase faults is similar in form to that for SG faults. However, the differential equation is only valid when the negative-sequence current is not suppressed by the RES. In the case of RES adopting a negative current suppression strategy, the differential equation can use the measured current of the faulted phase to replace $i_{\mathrm{F}\varphi\varphi}$ [17], i.e., $u_{M\varphi\varphi}\approx(R_1 i_{M\varphi\varphi}+L_1\mathrm{d}i_{M\varphi\varphi}/\mathrm{d}t)x+i_{M\varphi}R'_{\mathrm{F}}$.

The time-domain distance protection enables fast calculation of fault distance based on several sampling points. However, for engineering applications, it still presents certain challenges regarding the accuracy and robustness of the algorithm, especially for mixed lines. Thus, we denote (2) as the conventional algorithm.

B. Accuracy Analysis Under Inhomogeneous Line Parameters

The topologies of OHL and UGC are shown in Fig. 2(b) and (c), respectively. Because the spacing between the cable conductors is relatively closer, both the impedance magnitude and the impedance angle of the UGC are smaller in comparison with those of the OHL. Thus, the impedance per unit length differs significantly between the OHL and UGC sections of the mixed line. Therefore, for faults occurring at different locations on the mixed line, the actual unit impedance from the relay to the fault location is uncertain. In this paper, the actual unit impedance is denoted by $Z_1=|Z_1|\angle\theta_1=R_1+\mathrm{j}\omega L_1$, where θ_1 is the positive-sequence impedance angle of the transmission line; and ω is the fundamental angular frequency ($\omega=2\pi f$ and $f=50$ Hz). Meanwhile, the unit impedance in the distance relay is set based on the average impedance of the entire mixed line, which can be expressed as $Z_1^*=|Z_1^*|\angle\theta_1^*=R_1^*+\mathrm{j}\omega L_1^*$, where superscript $*$ denotes the average value of the line parameter (such as impedance) for the entire mixed line. The inequality between Z_1^* and Z_1 affects the location accuracy of the distance relay, which is analyzed as follows.

By taking the metallic SG fault as an example, the measured current compensated by the zero-sequence current is denoted as $i_{M\varphi z}$. Its time-domain function can be expressed as $i_{M\varphi z}=|\dot{I}_{M\varphi z}|\sin(\omega t)$, where $\dot{I}_{M\varphi z}$ is the fundamental-frequency current phasor, whose phase angle is taken as the reference angle. The zero-sequence measured current is expressed as $i_{M0}=|\dot{I}_{M0}|\sin(\omega t+\theta_{M0})$, where θ_{M0} is the phase angle of $\dot{I}_{M0}$. Based on (1), the measured voltage can be expressed as $u_{M\varphi}=p_{M\varphi}x=x|Z_1||\dot{I}_{M\varphi z}|\sin(\omega t+\theta_1)$. It is worth noting that the differential function $p_{M\varphi}$ is determined based on Z_1. In addition, based on Z_1^* set in the distance relay, the differential function used for the LSM calculation is $p^*_{M\varphi}=|Z_1^*||\dot{I}_{M\varphi z}|\cdot\sin(\omega t+\theta_1^*)$. By substituting the time-domain functions of $u_{M\varphi}$, $p^*_{M\varphi}$, and i_{M0}, the discretized (2) is expanded as (4). The derivation of (4) is based on trigonometric transformations and the substitution of integration for data summation. It should be noted that R_{F} is assumed to be 0 to analyze the effect of the inhomogeneous line parameters.

$$\hat{x}=(\boldsymbol{I}_{M\varphi}^{\mathrm{T}}\boldsymbol{I}_{M\varphi})^{-1}\boldsymbol{I}_{M\varphi}^{\mathrm{T}}\boldsymbol{U}_{M\varphi}|_{\phi}=\frac{\sum_{t=k_1\Delta t}^{k_n\Delta t}u_{M\varphi}(k_i)p^*_{M\varphi}(k_i)\sum_{t=k_1\Delta t}^{k_n\Delta t}(3i_{M0}(k_i))^2-\sum_{t=k_1\Delta t}^{k_n\Delta t}3i_{M0}(k_i)u_{M\varphi}(k_i)\sum_{t=k_1\Delta t}^{k_n\Delta t}3i_{M0}(k_i)p^*_{M\varphi}(k_i)}{\sum_{t=k_1\Delta t}^{k_n\Delta t}(p^*_{M\varphi}(k_i))^2\sum_{t=k_1\Delta t}^{k_n\Delta t}(3i_{M0}(k_i))^2-\left(\sum_{t=k_1\Delta t}^{k_n\Delta t}3i_{M0}(k_i)p^*_{M\varphi}(k_i)\right)^2}=$$

$$x\frac{|Z_1|}{|Z_1^*|}\frac{\sum_{t=k_1\Delta t}^{k_n\Delta t}\sin(\omega t+\theta_1)\sin(\omega t+\theta_1^*)\sum_{t=k_1\Delta t}^{k_n\Delta t}\sin^2(\omega t+\theta_{M0})-\sum_{t=k_1\Delta t}^{k_n\Delta t}\sin(\omega t+\theta_{M0})\sin(\omega t+\theta_1)\sum_{t=k_1\Delta t}^{k_n\Delta t}\sin(\omega t+\theta_{M0})\sin(\omega t+\theta_1^*)}{\sum_{t=k_1\Delta t}^{k_n\Delta t}\sin^2(\omega t+\theta_1^*)\sum_{t=k_1\Delta t}^{k_n\Delta t}\sin^2(\omega t+\theta_{M0})-\left(\sum_{t=k_1\Delta t}^{k_n\Delta t}\sin(\omega t+\theta_{M0})\sin(\omega t+\theta_1^*)\right)^2}=$$

$$x\frac{|Z_1|}{|Z_1^*|}\frac{\sin(\theta_1-\theta_{M0})}{\sin(\theta_1^*-\theta_{M0})}=x\frac{|Z_1|}{|Z_1^*|}(\cos(\theta_1-\theta_1^*)+\sin(\theta_1-\theta_1^*)\cot(\theta_1^*-\theta_{M0}))\approx x\cos(\theta_1-\theta_1^*)\frac{|Z_1|}{|Z_1^*|} \tag{4}$$

where $\sum_{k_i=k_1}^{k_n}(\cdot)$ denotes the summation of the data within k_1 to k_n; and ϕ is the first row of $\boldsymbol{U}_{M\varphi}$.

According to (4), the calculated fault distance through LSM $\hat{x}$ deviates from the actual fault distance x. For the mixed line, since the angle difference between Z_1 and Z_1^* is generally not more than 10°, $\cos(\theta_1-\theta_1^*)$ is much larger than $\sin(\theta_1-\theta_1^*)\cot(\theta_1^*-\theta_{M0})$, and the latter can be ignored. As a result, the accuracy of fault location is mainly affected by the magnitude and angle differences between Z_1 and Z_1^*. Firstly, the angle difference $\theta_1-\theta_1^*$ always reduces $\hat{x}$, which can lead to incorrect tripping of the protection under external faults. When θ_1 and θ_1^* are close, the ratio of $|Z_1|/|Z_1^*|$ determines whether $\hat{x}$ is larger or smaller than x. For example, for the relay at node M shown in Fig. 2(a), if the fault occurs at OHL, $|Z_{1,\mathrm{ohl}}|/|Z_1^*|$ is greater than 1, where the subscript ohl represents the parameter of OHL. The calculated fault distance is enlarged, which may cause the protection to refuse to trip. If the relay is installed at node N, when the fault occurs at UGC, the calculated fault distance is reduced because $|Z_{1,\mathrm{ugc}}|/|Z_1^*|$ is less than 1, where the subscript ugc represents the parameter of UGC.

Therefore, the inhomogeneity of line parameters reduces the accuracy of fault location, which possibly leads to the over- or under-reach problem.

C. "0/0" Problem Caused by Weak Signals

For 3-phase faults, all SG relays and phase-to-phase relays are activated to locate the fault. In this case, the second column of the current matrix $\boldsymbol{I}_{M\varphi}$ (i.e., i_{M0} for SG relays or $i_{M\varphi\varphi2}$ for phase-to-phase relays) is numerically close to 0. However, in practice, i_{M0} or $i_{M\varphi\varphi2}$ under 3-phase faults is a irregular and weak signal caused by noise or other disturbances, which negatively affects the performance of LSM calculation. By taking the SG relay as an example, the zero-sequence current can be written as $3i_{M0}=\varepsilon(t)$, where $\varepsilon(t)$ is a random signal with infinitesimal amplitude at time t. Under the influence of inhomogeneous line parameters, the discretized (2) can be expanded as:

$$\begin{cases}\hat{x}=(\boldsymbol{I}_{M\varphi}^{\mathrm{T}}\boldsymbol{I}_{M\varphi})^{-1}\boldsymbol{I}_{M\varphi}^{\mathrm{T}}\boldsymbol{U}_{M\varphi}|_{\phi}=\dfrac{x|Z_1|}{|Z_1^*|}\dfrac{\sum_{t=k_1\Delta t}^{k_n\Delta t}\sin(\omega t+\theta_1)\sin(\omega t+\theta_1^*)\sum_{t=k_1\Delta t}^{k_n\Delta t}\varepsilon^2(t)-\sum_{t=k_1\Delta t}^{k_n\Delta t}\varepsilon(t)\sin(\omega t+\theta_1)\sum_{t=k_1\Delta t}^{k_n\Delta t}\varepsilon(t)\sin(\omega t+\theta_1^*)}{\sum_{t=k_1\Delta t}^{k_n\Delta t}\varepsilon(t)\sin(\omega t+\theta_1^*)\sum_{t=k_1\Delta t}^{k_n\Delta t}\varepsilon^2(t)-\left(\sum_{t=k_1\Delta t}^{k_n\Delta t}\varepsilon(t)\sin(\omega t+\theta_1^*)\right)^2}\\ \hat{R}_{\mathrm{F}}'=(\boldsymbol{I}_{M\varphi}^{\mathrm{T}}\boldsymbol{I}_{M\varphi})^{-1}\boldsymbol{I}_{M\varphi}^{\mathrm{T}}\boldsymbol{U}_{M\varphi}|_{\phi'}=x|Z_1||\dot{I}_{M\varphi}|\dfrac{\sum_{t=k_1\Delta t}^{k_n\Delta t}\varepsilon(t)\sin(\omega t+\theta_1)\sum_{t=k_1\Delta t}^{k_n\Delta t}\sin^2(\omega t+\theta_1^*)-\sum_{t=k_1\Delta t}^{k_n\Delta t}\sin(\omega t+\theta_1)\sin(\omega t+\theta_1^*)\sum_{t=k_1\Delta t}^{k_n\Delta t}\varepsilon(t)\sin(\omega t+\theta_1^*)}{\sum_{t=k_1\Delta t}^{k_n\Delta t}\varepsilon(t)\sin(\omega t+\theta_1^*)\sum_{t=k_1\Delta t}^{k_n\Delta t}\varepsilon^2(t)-\left(\sum_{t=k_1\Delta t}^{k_n\Delta t}\varepsilon(t)\sin(\omega t+\theta_1^*)\right)^2}\end{cases} \tag{5}$$

where ϕ' is the second row of $\boldsymbol{U}_{M\varphi}$.

As shown in (5), the numerator and denominator of the fractional term in the expression of $\hat{x}$ are both close to infinitesimals. If the angles of Z_1 and Z_1^* are the same (namely, $\theta_1=\theta_1^*$), the numerator and denominator are equal infinitesimals, and $\hat{x}=x|Z_1|/|Z_1^*|$. Otherwise, the numerator and denominator are unequal infinitesimals, and their values can vary with time because $\varepsilon(t)$ is a random signal. In this case, the calculated values of $\hat{x}$ cannot converge and can become outliers that deviate far from the actual fault distance. In addition, for the calculated fault resistance $\hat{R}_{\mathrm{F}}'$, it equals to 0 when $\theta_1=\theta_1^*$ (for metallic 3-phase faults). However, when $\theta_1\neq\theta_1^*$, the magnitude of the numerator (proportional to $\varepsilon(t)$) is much larger than the magnitude of the denominator (proportional to $\varepsilon^2(t)$), which results in a huge calculation error in $\hat{R}_{\mathrm{F}}'$.

As a result, when the zero-sequence or the negative-sequence current is a weak signal, the mismatched impedance angles can cause the calculation results to be no longer convergent and rational. For internal 3-phase faults at the mixed line, θ_1 is always not equal to θ_1^*, and the calculation outliers can significantly reduce the operational reliability of the protection. In addition, when a 3-phase fault occurs outside the protected line, θ_1 is usually not equal to θ_1^*. The unreliable calculated fault distance may enter the action zone and cause the protection to trip incorrectly. Even in the case of normal power system operation, the "0/0" problem can lead to an erroneous tripping once the protection is activated by any disturbance. To avoid these problems, a fault resistance threshold can be used to block the relay. However, for internal 3-phase faults at the mixed lines, and in addition to the calculation outliers for $\hat{x}$, the calculated value of $\hat{R}_{\mathrm{F}}'$ can easily exceed thousands of ohms above the resistance threshold. In this case, the distance relay has a high probability of being blocked and refusing to trip. Therefore, the robustness of the conventional algorithm is extremely poor.

In conclusion, for time-domain distance protection, the accuracy of the calculated fault distance and the reliability of the conventional algorithm can be seriously affected by the inhomogeneous line parameters.

III. Protection Algorithm with High Robustness and Accuracy

A. Singular Value Decomposition-based LSM (SVD-LSM)

In this paper, the SVD-LSM is utilized to solve the system with differential equations. The SVD-LSM is immune to invalid signals and noise, thus avoiding the "0/0" problem caused by weak signals. Figure 3 shows the calculation steps of SVD-LSM for the SG relay, where $\boldsymbol{D}$ is an $n\times2$ matrix; $\boldsymbol{S}$ is a 2×2 diagonal matrix with non-negative diagonal entries; $\boldsymbol{V}$ is a 2×2 orthogonal matrix; $\boldsymbol{d}_1$ and $\boldsymbol{d}_2$ are the col-

umns of $\boldsymbol{D}$; $\boldsymbol{v}_1$ and $\boldsymbol{v}_2$ are the columns of $\boldsymbol{V}$; and σ_1 and σ_2 are the diagonal entries of $\boldsymbol{S}$, which are the singular values of $\boldsymbol{I}_{M\varphi}$.

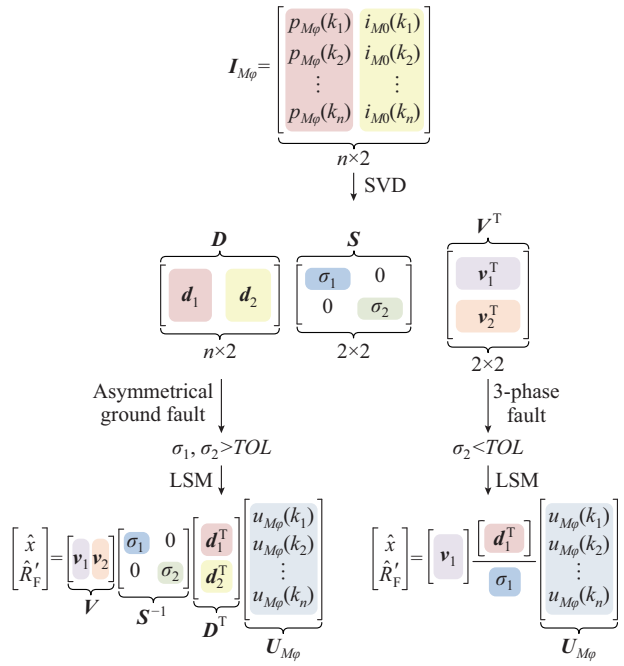

Fig. 3. Calculation steps of SVD-LSM for SG relay.

First, the $n\times 2$ current matrix $\boldsymbol{I}_{M\varphi}$ is decomposed by SVD, i.e., $\boldsymbol{I}_{M\varphi}=\boldsymbol{DSV}^{\mathrm{T}}$. In the next step, the singular values smaller than the set tolerance *TOL* can be considered as 0. Note that *TOL* can be set according to the minimum precision of the protection algorithm. In this paper, the singular values are float-type variables with 6 to 7 significant digits after the decimal point, so *TOL* can be set as 10^{-3}-10^{-4}.

When an asymmetrical ground fault occurs, the differential function $p_{M\varphi}$ and the zero-sequence current i_{M0} are both signals with a certain amplitude. In this situation, both the singular values σ_1 and σ_2 of $\boldsymbol{I}_{M\varphi}$ are greater than *TOL*, and the fault distance is calculated by SVD-LSM as:

$$[\hat{x}\quad \hat{R}_{\mathrm{F}}']^{\mathrm{T}}=\boldsymbol{VS}^{-1}\boldsymbol{D}^{\mathrm{T}}\boldsymbol{U}_{M\varphi} \tag{6}$$

The calculation of (6) is equivalent to the conventional algorithm based on LSM. Thus, according to (4), $\hat{x}$ approximately equals to γx, where $\gamma=\cos(\theta_1-\theta_1^*)|Z_1|/|Z_1^*|$.

In particular, when a 3-phase fault occurs, i_{M0} is a weak signal. Thus, the magnitude of σ_2 is close to infinitesimal. In this case, the matrices $\boldsymbol{D}$ and $\boldsymbol{V}$ retain only the first columns $\boldsymbol{d}_1$ and $\boldsymbol{v}_1$. Thus, the fault distance is calculated as:

$$[\hat{x}\quad \hat{R}_{\mathrm{F}}']^{\mathrm{T}}=\boldsymbol{v}_1\sigma_1^{-1}\boldsymbol{d}_1^{\mathrm{T}}\boldsymbol{U}_{M\varphi} \tag{7}$$

In addition, (7) is equivalent to omitting the second column of $\boldsymbol{I}_{M\varphi}$, so the discretized (7) can be further expanded as (8). For the first term γx in (8), it is a fixed value and is equal to the calculated fault distance under SG faults. As for the second term, it is a periodical time-varying error with a period of $T/2$, where T is the period of fundamental frequency signals ($T=20$ ms). Although the calculated fault distances through SVD-LSM are no longer outliers, the mismatch between θ_1 and θ_1^* still leads to a time-varying error in $\hat{x}$, unless $T_{\mathrm{w}}=mT/2$, where m can be any positive interger. The appropriate minimum value of T_{w} is 10 ms, which allows $\hat{x}$ to converge to the fixed distance γx under 3-phase faults. However, the long time window limits the protection operation speed under SG faults. In such cases, no matter how long T_{w} is, $\hat{x}$ is able to converge to γx. Therefore, in order to realize the fast fault identification during the RES transient stage, it is necessary to overcome the non-convergence problem of the short time window calculation. Moreover, compared with the LSM as (2), the SVD-LSM in (6) and (7) simplifies the computation, thereby improving the program efficiency.

$$\hat{x}=\frac{\sum_{k_i=k_1}^{k_n}u_{M\varphi}p_{M\varphi}^*}{\sum_{k_i=k_1}^{k_n}(p_{M\varphi}^*)^2}=\frac{x|Z_1|}{|Z_1^*|}\frac{\sum_{t=k_1\Delta t}^{k_n\Delta t}\sin(\omega t+\theta_1)\sin(\omega t+\theta_1^*)}{\sum_{t=k_1\Delta t}^{k_n\Delta t}\sin^2(\omega t+\theta_1^*)}=\underbrace{\frac{x|Z_1|}{|Z_1^*|}\cos(\theta_1-\theta_1^*)}_{\gamma x}-\underbrace{\frac{x|Z_1|}{|Z_1^*|}\frac{\sin(\omega T_{\mathrm{w}})\sin(\theta_1-\theta_1^*)\sin(2\omega t-\omega T_{\mathrm{w}}+2\theta_1^*)}{\sin(\omega T_{\mathrm{w}})\cos(2\omega t-\omega T_{\mathrm{w}}+2\theta_1^*)-\omega T_{\mathrm{w}}}}_{\text{periodic time-varying error of }\hat{x}} \tag{8}$$

B. Weighting Method Based on Euclidean Norm

To enhance the convergence of the protection algorithm, the calculated fault distances through SVD-LSM are assigned weights to indicate their confidence level. By substituting $\hat{x}$ and $\hat{R}_{\mathrm{F}}'$ back into (1), the weight w can be defined as:

$$w=\frac{1}{E}=\frac{1}{\|\boldsymbol{U}_{M\varphi}-\boldsymbol{I}_{M\varphi}[\hat{x}\quad \hat{R}_{\mathrm{F}}']^{\mathrm{T}}\|} \tag{9}$$

where E is the Euclidean norm of the difference between $\boldsymbol{U}_{M\varphi}$ and $\boldsymbol{I}_{M\varphi}[\hat{x},\hat{R}_{\mathrm{F}}']^{\mathrm{T}}$.

The smaller E is, the better $\hat{x}$ and $\hat{R}_{\mathrm{F}}'$ satisfy (1). Thus, $\hat{x}$ with large weight is relatively more convincing. Accordingly, the calculated fault distance can be continuously weighted based on the latest $\hat{x}$ and the corresponding w, i.e.,

$$x_{\mathrm{e}}(k_i)=\frac{w_{\mathrm{e}}(k_{i-1})x_{\mathrm{e}}(k_{i-1})+w\hat{x}}{w_{\mathrm{e}}(k_{i-1})+w} \tag{10}$$

where x_{e} is the weighted distance and its own weight is denoted by w_{e}. After the protection is activated, x_{e} is continuously updated for every SVD-LSM calculation. In addition, w_{e} is also updated according to $w_{\mathrm{e}}(k_i)=w_{\mathrm{e}}(k_{i-1})+w$.

According to (8), the SVD-LSM calculation results of $\hat{x}$ under 3-phase faults are shown in Fig. 4. The adopted time windows are set as 1, 5, and 10 ms, respectively. Furthermore, according (10), the weighted distance x_{e} for $\hat{x}$ with $T_{\mathrm{w}}=1$ ms is shown as the red line in Fig. 4(a). Note that Fig. 4(a) displays the relative values of the calculated fault distance $\hat{x}$ to the actual fault distance x.

Obviously, the SVD-LSM calculation results are no longer irregular outliers under the 3-phase faults, but $\hat{x}$ still fails to converge due to the periodic fluctuations. Even if the difference between θ_1 and θ_1^* is only 5°, the fluctuation can exceed 40% of the actual fault distance x.

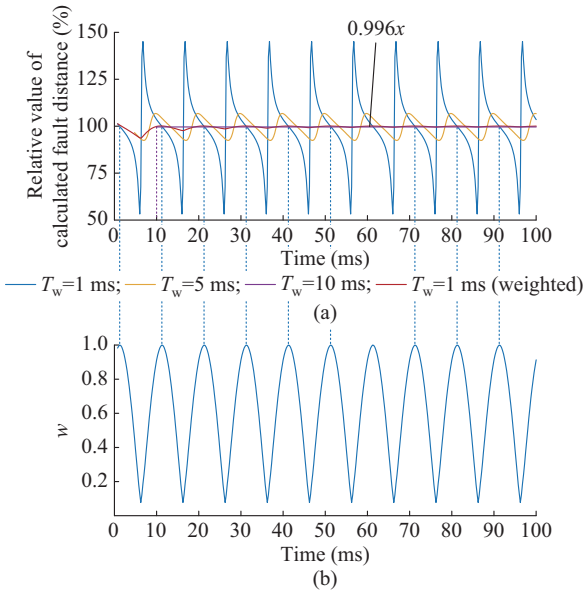

Fig. 4. SVD-LSM calculation results of $\hat{x}$ under 3-phase faults ($|Z_1^*|=|Z_1|$, $\theta_1^*=70°$, and $\theta_1=75°$). (a) Relative value of calculated fault distance for different time windows. (b) Weight for $T_w=1$ ms.

Of course, as T_w increases, the fluctuation gradually decreases, which allows $\hat{x}$ to tend to converge. In particular, when $T_w=10$ ms, $\hat{x}$ can fully converge to $0.996x$ ($\gamma=\cos(\theta_1-\theta_1^*)|Z_1|/|Z_1^*|=99.6\%$ in this case). However, the SVD-LSM obtains the first $\hat{x}$ within 10 ms after the fault occurrence. As for $\hat{x}$ with $T_w=1$ ms, its confidence level is evaluated by the weight defined in (9), as shown in Fig. 4(b). The weight is relatively large when $\hat{x}$ is close to $0.996x$, while it is small for the $\hat{x}$ with a large fluctuation. Based on this, the weighted distance x_e can also converge to $0.996x$ in about 10 ms. Therefore, the proposed weighting method breaks the limitation of the time window under 3-phase faults, and can obtain convergent fault distances after a period of weighting. For asymmetrical faults, the proposed weighting method can retain the advantages of the short time window and quickly obtain reliable fault distances.

C. Distance Correction Method for Mixed Lines

According to the above analysis, the weighted distance x_e can converge to γx under both SG faults and 3-phase faults. However, the inhomogeneous line parameters still cause x_e to differ from the actual fault distance, especially for lines with mixed OHLs and UGCs. To obtain the exact fault location, the calculated fault distance can be corrected according to the specific parameters of different sections of the mixed line. By using the distance relay on *M*-side (at node *M*) as an example, as shown in Fig. 2(a), the weighted distance x_e needs to be corrected as:

$$x_m=\begin{cases}\dfrac{x_e}{\gamma_{ohl}} & 0<x_e\le\gamma_{ohl}l_{ohl}\\ l_{ohl}+\dfrac{x_e-\gamma_{ohl}l_{ohl}}{\gamma_{ugc}} & \gamma_{ohl}l_{ohl}<x_e<l_{MN}\\ x_e & x_e\le 0\bigcup x_e\ge l_{MN}\end{cases}\tag{11}$$

where x_m is the corrected weighted distance used for fault identification; $l_{MN}=l_{ohl}+l_{ugc}$ is the total length of the mixed line; and γ_{ohl} and γ_{ugc} are the correction coefficients for the OHL and UGC, respectively. The correction coefficients can be determined by:

$$\begin{cases}\gamma_{ohl}=\cos(\theta_{1,ohl}-\theta_1^*)\dfrac{|Z_{1,ohl}|}{|Z_1^*|}\\ \gamma_{ugc}=\cos(\theta_{1,ugc}-\theta_1^*)\dfrac{|Z_{1,ugc}|}{|Z_1^*|}\end{cases}\tag{12}$$

Furthermore, for mixed lines consisting of multiple segments of OHL and UGC, the idea of correcting x_e, as in (11), increases the implementation steps and the complexity of the protection algorithm. Therefore, an alternative approach for time-domain distance protection of mixed lines is to adjust the distance threshold to ensure an accurate protection range. Still using the distance relay on *M*-side in Fig. 2 (a) as an example, the protection area of the mixed line is set as $x_{set}=k_{rel}l_{MN}$, where x_{set} is the distance threshold; and k_{rel} is the reliability coefficient, which is usually taken as 70%-90%. To ensure that the protection can work accurately, the distance threshold can be corrected as:

$$x_{set}^*=\gamma_{ohl}l_{ohl}+\left(k_{rel}-\frac{l_{ohl}}{l_{MN}}\right)\gamma_{ugc}l_{ugc}\tag{13}$$

where x_{set}^* is the corrected distance threshold for mixed lines.

D. Protection Algorithm

By combining the above-mentioned methods, the flow chart of the protection algorithm is illustrated in Fig. 5. The following are the implementation steps.

Step 1: initialize the distance relay when the protection is started. The initial value of weighted distance x_e is set to be 999 km, and its own weight w_e is set to be 0.

Step 2: read the sampling data of measured voltage and current, calculate the differential function of the sampled current, and form the matrices as (3).

Step 3: perform a singular value decomposition of the current matrix $\boldsymbol{I}_{M\varphi}$, and calculate $\hat{x}$ and $\hat{R}_F'$ according to (6) or (7) based on the obtained singular values.

Step 4: first, assign a weight w to the calculated fault distance $\hat{x}$ based on the Euclidean norm of $\boldsymbol{U}_{M\varphi}-\boldsymbol{I}_{M\varphi}[\hat{x},\hat{R}_F']$. Then, update the weighted distance as $x_e(k_i)=(w_e(k_{i-1})x_e(k_{i-1})+w\hat{x})/(w_e(k_{i-1})+w)$. Finally, update weight of x_e as $x_e(k_i)=w_e(k_{i-1})+w$.

Step 5: judge whether x_e is convergent. It is essential to assess the convergence of the weighted distance to guarantee the operation reliability of the protection. For example, if the difference in weighted distances is less than 0.1 km within 3 ms, the weighted distance is considered convergent and proceed to *Step 6*, otherwise return to *Step 2*.

Step 6: correct the weighted distance according to (11).

Step 7: if x_m is within the range of $(-1,x_{set})$, go to *Step 8*; otherwise the fault is recognized as an external fault. The lower limit can be set as −1 to avoid the dead zone under near-end internal faults.

Step 8: in order to avoid incorrect tripping under near-end backward faults, a fault directional criterion is required. In this paper, a backward fault blocking criterion is proposed for RES-side protection.

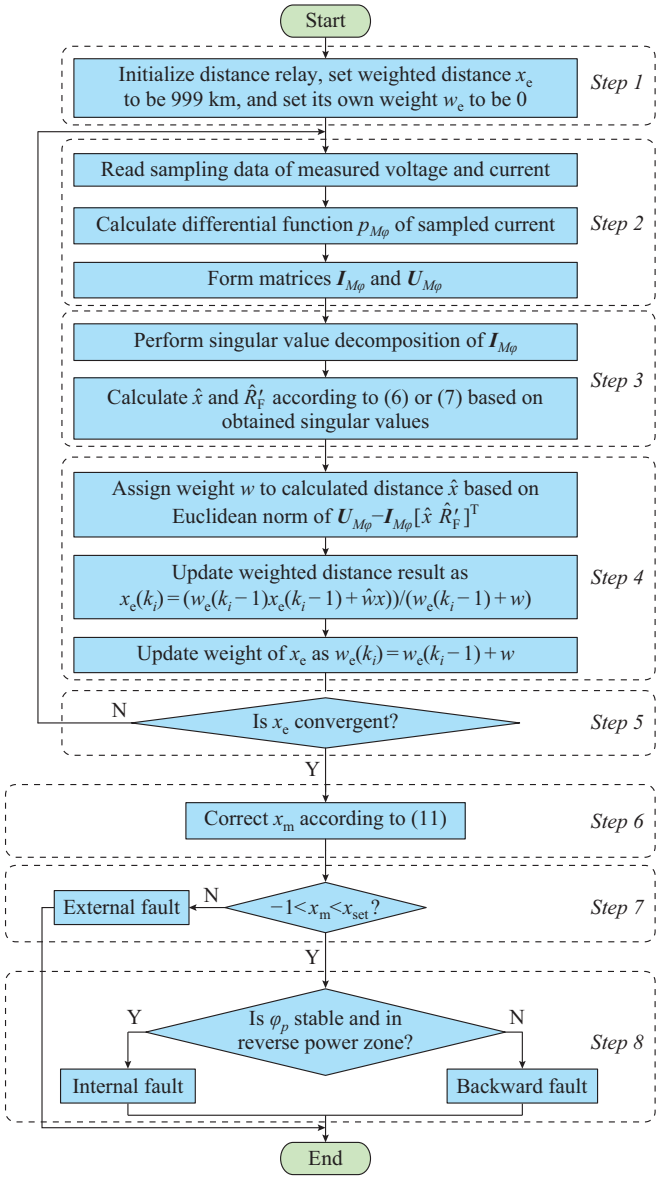

Fig. 5. Flow chart of protection algorithm.

The protection is blocked when the power factor angle φ_p (the angle difference between the measured voltage and current) remains stable in the reverse power zone. If φ_p is in the range of 105°-345° and changes less than 3° in the last 3 ms, the fault direction is detected as backward and the protection is blocked, otherwise the protection normally sends the trip signal. In addition, when the measured voltage is less than $0.1U_N$ (U_N is the rated voltage), the memory voltage should be used to obtain the power factor angle.

The backward fault blocking criterion is further explained as follows. For RES-side protection, when the fault direction is forward, the short-circuit current is supplied by the RES. In this case, the measured φ_p can fluctuate significantly throughout the fault transient period (tens of milliseconds). In addition, φ_p is affected by the low voltage ride-through (LVRT) strategy of the RES. The fault direction cannot be accurately and reliably identified from φ_p. However, when the fault direction is backward, the short-circuit current is supplied by the grid, and the measured φ_p remains stable in the reverse power zone. Therefore, the protection algorithm proposed in this paper, which is the combination of the SVD-LSM, the weighting method, and the distance correction method, can reliably block the distance protection under near-end backward faults.

In summary, by introducing SVD-LSM, the protection algorithm avoids the calculation outliers caused by the "0/0" problem. The weighting method solves the problem of computational non-convergence when adopting a short time window, thus maintaining the fast operation of the protection. As a result, the robustness of the protection is greatly enhanced. Therefore, the protection algorithm proposed in this paper is referred to as the robust algorithm, and it is abbreviated as the proposed algorithm in the following. In addition, the distance correction method improves the accuracy of fault location, thus overcoming the possible over- or under-reach of the protection on mixed lines.

IV. Experimental Test

A. Experimental Test Platform

Based on the hardware platform in [22], the proposed algorithm is implemented in a prototype of the protection device. The real-time digital simulator (RTDS) platform is used to conduct hardware-in-the-loop (HIL) tests for the prototype of the protection device. The physical layout of the experimental test platform is illustrated in Fig. 6. In the RTDS platform, a detailed model of the renewable power transmission system with mixed lines is built, the topology of the simulation model is shown in Fig. 7. The relevant parameters are shown in Supplementary Material A Table SAI.

B. Performance of Prototype of Protection Device

1) Asymmetrical Faults

The length of both OHL and UGC sections of the mixed line is 15 km. Thus, the distance threshold is set to be $x_{set}=0.8l_{MN}=24$ km. The unit time window is set to be $T_w=2.5$ ms, indicating that 10 sampling points (at a sampling rate of 4 kHz) are required in an SVD-LSM to construct the matrices shown in (3). To verify the accuracy of fault location of the proposed algorithm under inhomogeneous line parameters, two AG faults are set at f_3 ($x=23.4$ km, internal fault) and f_4 ($x=24.6$ km, external fault), respectively. In addition, the fault instant is set to be 50 ms. During the fault period, the inverter of the DFIG controls the output positive-sequence current according to the fault LVRT strategy, i. e., $\Delta I_1=K_1(0.9-U_1)I_N$, where ΔI_1 is the increase in the output positive-sequence reactive current of the DFIG; I_N is the rated current; K_1 is the proportional coefficient; and U_1 is the voltage at the point of common coupling (PCC). It is worth noting that the negative-sequence current suppression strategy is not adopted in the DFIG. The recorded data under two AG faults are shown in Figs. 8 and 9, respectively, where t_{OP} is the protection operation time, which is from the time when the fault occurs to that the trip signal is received by the RTDS platform. For comparison, the calculated fault distance through conventional algorithm in (2) is also shown.

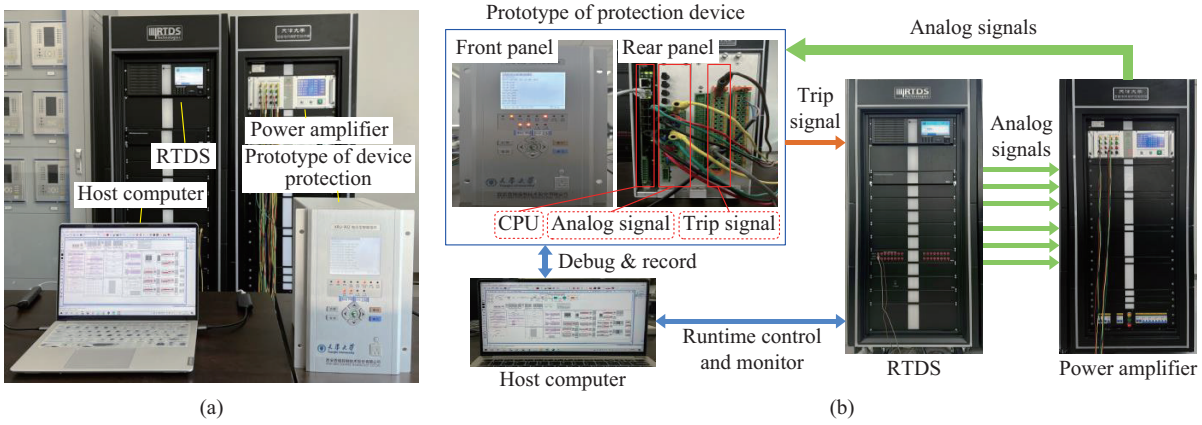

Fig. 6. Physical layout of experimental test system. (a) Physical diagram. (b) Connection diagram.

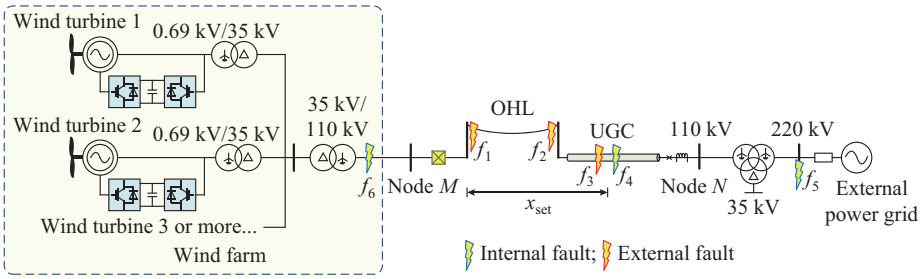

Fig. 7. Topology of simulation model.

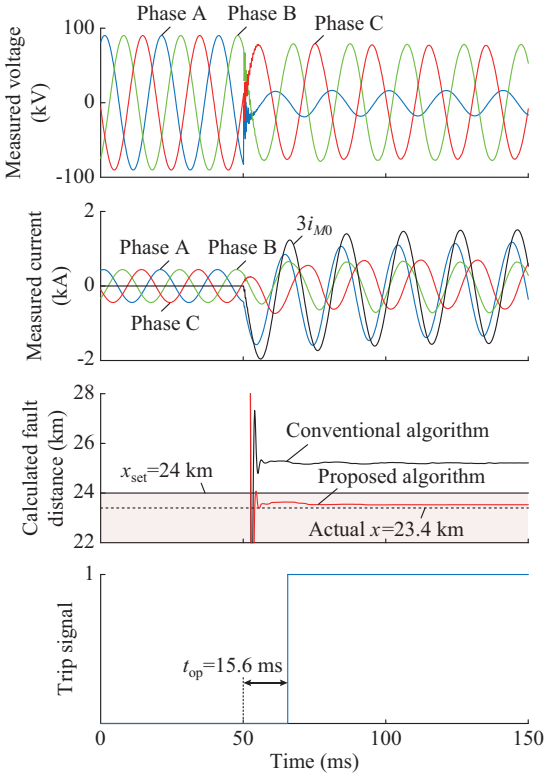

Fig. 8. Recorded data of AG fault at f_3 (23.4 km).

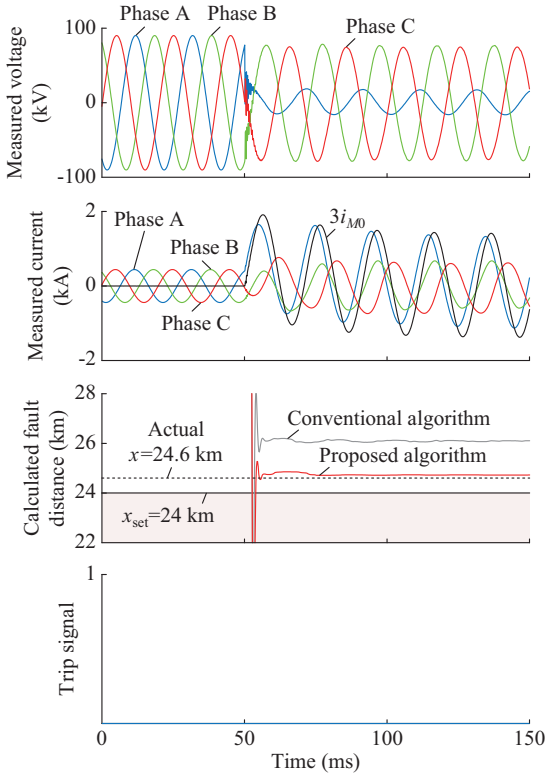

Fig. 9. Recorded data of AG fault at f_4 (24.6 km).

As shown in Figs. 8 and 9, the calculated fault distances through conventional algorithm are about 25.2 km (fault at f_3) and 26.1 km (fault at f_4), which are both larger than the actual fault distances. This is because the unit impedance from node M to the fault location is greater than the average impedance of the mixed line. The mismatched impedance causes the conventional algorithm to refuse to trip under the internal fault at f_3. Differently, based on the distance correc-

tion method, the calculated fault distances through the proposed algorithm are about 23.5 km (fault at f_3) and 24.7 km (fault at f_4), which are much closer to the actual fault distances. The accurate results ensure that the prototype of the protection device operates correctly even under faults near x_{set}, and avoids over- or under-reach under the effect of inhomogeneous line parameters. Therefore, the proposed algorithm has better accuracy and selectivity of fault location under asymmetrical faults compared with the conventional algorithm.

It should be pointed out that in the presence of uncontrolled zero-sequence current, the controlled positive-sequence current has less effect on the fault characteristics. As can be observed from Figs. 8 and 9, the measured currents of phase A are mainly characterized by the zero-sequence currents. In this situation, the prototype of the protection device is basically unaffected by the LVRT strategy of the DFIG. However, the limited amplitude of the RES-side short-circuit current still amplifies the impact of the fault resistance, so the protection capability against fault resistance is further tested and analyzed in Section IV-C.

2) 3-phase Faults

To test the robustness of the protection, 3-phase faults are set at f_2 (end of OHL, $x=15$ km) and f_5 (220 kV busbar of the terminal substation, which is connected to the external power grid), respectively. When the severe 3-phase fault occurs, the crowbar is immediately engaged, and the short-circuit current of DFIG can contain an obvious transient component of non-fundamental frequency [22]. The recorded data under two faults are given in Figs. 10 and 11. For comparison, the calculated fault distance and resistance through the conventional algorithm in (2) are also shown.

As shown in Figs. 10 and 11, the calculated fault distances through the conventional algorithm are non-convergent outliers for both faults at f_2 on the mixed line and at f_5 outside the mixed line. This is because the zero-sequence current is an irregular infinitesimal signal under these two faults, and the actual impedance angle is not the same as the impedance angle set in the relay, resulting in one infinitesimal being divided by another different infinitesimal during the calculation. In addition, the calculated fault resistances may reach several kΩ to tens of kΩ, which is far from the actual fault resistance. In such cases, it is difficult to guarantee that the conventional algorithm can reliably trip under internal fault at f_2 and remain non-tripping under external fault at f_5. In contrast, the calculated fault distance through the proposed algorithm converges to 15 km within 10 ms so that the protection is able to trip reliably and quickly under fault at f_2. Under fault at f_5, the proposed algorithm also obtains a convergent fault location result, which ensures that the protection does not trip. Therefore, the proposed algorithm eliminates the "0/0" problem caused by weak signals and has better robustness when applied to mixed lines.

In addition, as can be observed from Figs. 10 and 11, the frequencies of the measured currents are about 65 Hz. Despite the significant change in the frequency characteristic, the proposed algorithm can still obtain convergent and stable distance results during the transient stage of the DFIG. This is because the differential equations in the proposed algorithm are valid for currents of any frequency.

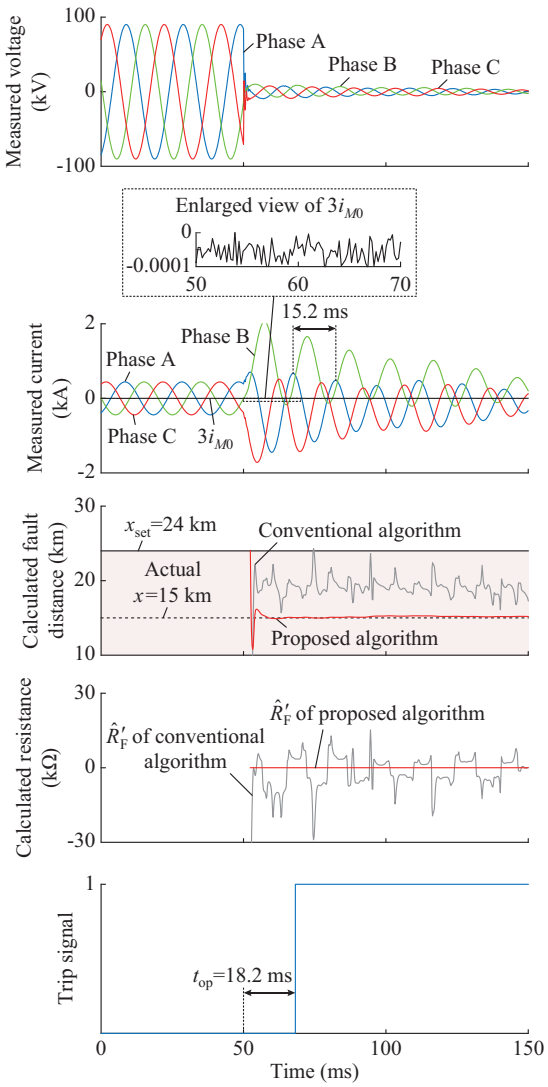

Fig. 10. Recorded data of 3-phase fault at f_2 (15 km).

Furthermore, to demonstrate the respective roles of SVD-LSM, the weighting method, and the distance correction method, Fig. 12 shows the calculated fault distance through different methods under the 3-phase fault at f_2.

Obviously, compared with LSM, SVD-LSM eliminates the irregular outliers, but its calculated fault distances still fluctuate periodically, and the fluctuation is related to the time window. When $T_w=2.5$ ms, the calculated fault distance fluctuates drastically with a range over 4 km. When $T_w=5$ ms, the calculated fault distance still fluctuates. It is only when $T_w=10$ ms that the calculated fault distance converges to about 19 km at 15 ms after the fault. In contrast, even with a 2.5 ms time window, the weighting method can make the weighted distance converge to about 19 km at 10 ms after the fault. Therefore, the weighting method greatly improves the convergence of the proposed algorithm while maintaining the fast operation speed of the protection. Finally, the distance correction method can correct the obtained distance to about 15 km, which ensures the accuracy of fault location under the effect of inhomogeneous line parameters.

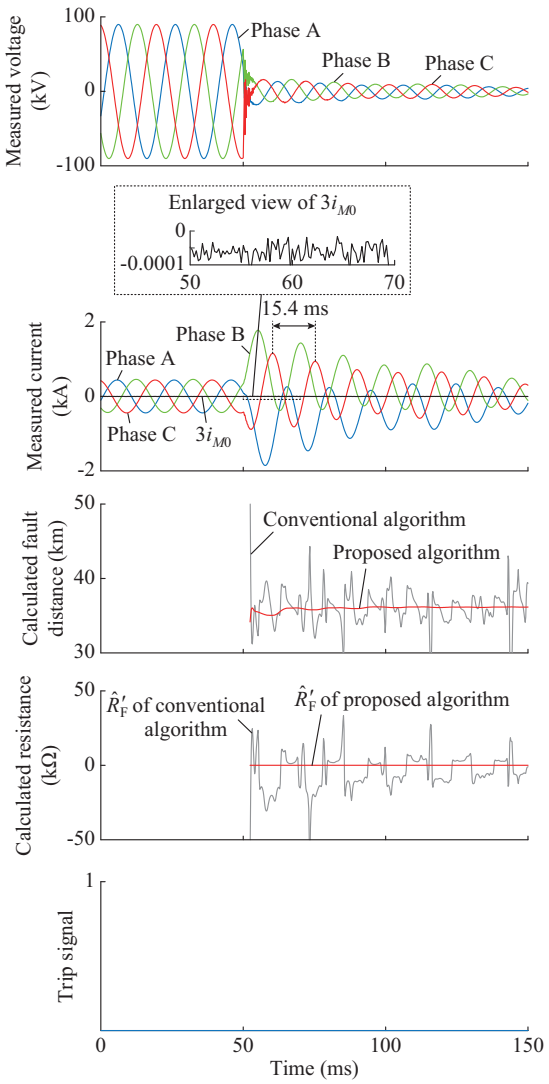

Fig. 11. Recorded data of 3-phase fault at f_5 (220 kV busbar).

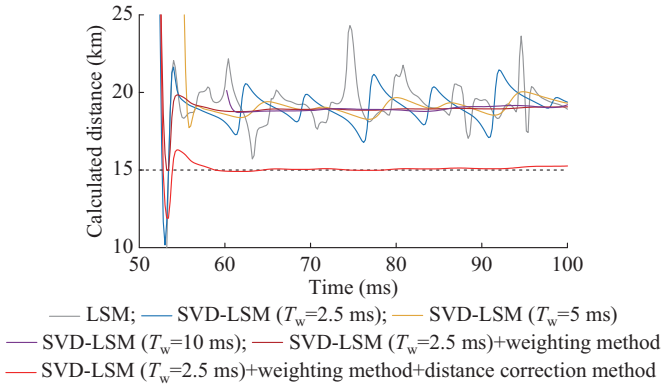

Fig. 12. Calculated fault distances through different methods under 3-phase fault at f_2.

3) Near-end Faults

To verify the protection performance under near-end faults, 3-phase faults are set at f_1 (start of OHL, $x=0$) and f_6 (backward fault), respectively. The recorded data of two faults are shown in Figs. SA1 and SA2 in Supplementary Material A, where the calculated fault distances for two near-end faults are both close to zero, regardless of whether the fault direction is forward or backward. If a protection range of $(0, x_{set})$ is adopted, there could be a dead zone. In addition, the measured power factor angle fluctuates significantly for the fault at f_1 under the influence of RESs, while it quickly converges to a stable value (261°, in the reverse power zone) for the fault at f_6. Therefore, by selecting the protection range as $(-1, x_{set})$ and adopting the backward fault blocking criterion, the protection can trip quickly for the internal fault at f_1 and be reliably blocked for the backward fault at f_6.

4) Different Fault Conditions

In this part, the faults under different fault conditions are set to test the protection performance. The experiment is repeated five times under each fault condition, and the recorded data are shown in Table I. It is worth noting that the tripping relay operation time in Table I is about 6-8 ms.

TABLE I
RECORDED DATA UNDER DIFFERENT FAULT CONDITIONS

Internal/external fault	Fault location	Fault type	x_m (km)	t_{op} (ms)
Internal fault	f_1 (0)	AG	0.0-0.1	13.6-14.2
		AB	0.0-0.2	13.6-15.0
		ABG	0.0-0.3	13.2-13.8
		ABC	−0.1-0.4	13.6-14.2
	f_2 (15 km)	AG	14.6-15.0	15.7-18.7
		AB	14.6-15.0	15.6-18.9
		ABG	14.6-15.0	15.4-18.4
		ABC	14.5-15.3	16.4-21.2
	f_3 (23.4 km)	AG	23.1-23.6	15.6-19.9
		AB	23.1-23.5	15.0-19.4
		ABG	22.9-23.5	14.8-19.3
		ABC	22.6-23.5	16.8-23.0
External fault	f_4 (24.6 km)	AG	24.3-25.0	
		AB	24.3-24.9	
		ABG	24.3-25.1	
		ABC	24.1-25.4	
	f_5 (220 kV busbar)	AG	47.9-49.6	
		AB	34.8-35.4	
		ABG	34.5-35.8	
		ABC	34.2-36.0	
	f_6 (backward fault)	AG	−0.1-0.0	Blocked
		AB	−0.2-0.0	Blocked
		ABG	−0.1-0.0	Blocked
		ABC	−0.2-0.0	Blocked

For the faults at f_1-f_4 on the mixed line, the calculated fault distances are close to the actual fault distances. The maximum errors is less than 0.5 km under asymmetrical faults and less than 0.8 km under 3-phase faults, respectively. Therefore, the prototype of the protection device can trip accurately and reliably under internal faults at f_1-f_3, independent of mixed OHL and UGC. For AG, AB, and ABG faults, the protection operation time is 13-20 ms. This implies that the proposed algorithm is able to recognize internal asymmetrical faults in about 7-14 ms (excluding the operation

time of the tripping relay). Even under the 3-phase faults at f_3 (which is near the end of the protection zone), the proposed algorithm is still able to detect the internal 3-phase fault within 17 ms (t_{op} is less than 23 ms). In addition, under the external faults at f_4 and f_5, the calculated fault distances are outside the action zone $(-1, x_{set})$. Under the backward faults at f_6, although the calculated fault distances are within the action zone $(-1, x_{set})$, the backward fault blocking criterion can reliably block the protection. Thus, the prototype of the protection device can be reliably prevented from tripping under external faults, which confirms the selectivity of the protection.

When the fault occurs at f_5 (the fault type is AB or ABG), the protection usually obtains the phase-to-phase fault distance according to the differential equation $u_{M\varphi\varphi}=(R_1 i_{M\varphi\varphi}+L_1 \mathrm{d}i_{M\varphi\varphi}/\mathrm{d}t)x$. Since the fault impedance includes the impedance of the mixed line and the substation main transformer, the calculated fault distance is the equivalent distance from node M to the 220 kV busbar, i. e., $x_m \approx (Z_1^* l_{MN}+Z_{T1})/Z_1^*$, where Z_{T1} is the impedance of the substation main transformer. Under the 3-phase fault, regardless of whether the proposed algorithm obtains the phase-to-phase fault distance according to $u_{M\varphi\varphi}=(R_1 i_{M\varphi\varphi}+L_1 \mathrm{d}i_{M\varphi\varphi}/\mathrm{d}t)x$ or the phase-to-ground fault distance according to $u_{M\varphi}=(R_1 i_{M\varphi}+L_1 \mathrm{d}i_{M\varphi}/\mathrm{d}t)x$ (the zero-sequence current is approximately 0), the calculated fault distance can still be expressed as $x_m \approx (Z_1^* l_{MN}+Z_{T1})/Z_1^*$. Differently, when the AG fault occurs, the proposed algorithm obtains the phase-to-ground fault distance based on the differential equation $u_{M\varphi}=[R_1(i_{M\varphi}+K_R 3i_{M0})+L_1 \mathrm{d}(i_{M\varphi}+K_L 3i_{M0})/\mathrm{d}t]x$, where the measured current needs to be compensated by i_{M0}. However, the zero-sequence compensation coefficients K_R and K_L are determined by the sequence impedances of the mixed line, and do not match the relationship between the sequence impedances of the substation main transformer. Due to the errors in the zero-sequence compensation coefficients, the calculated fault distance is no longer the equivalent distance from node M to 220 kV busbar, i. e., $x_m \neq (Z_1^* l_{MN}+Z_{T1})/Z_1^*$. Therefore, there is a difference in x_m between the AG fault and other fault types.

C. Other Impact Factors

1) Impact of Fault Resistance

To test the protection capability against the fault resistance, AG faults are set at f_2 ($x=15$ km) with various fault resistances (5-25 Ω). Figure 13 shows the calculated fault distances under AG faults at f_2 with various fault resistances.

The increase in the error of calculated fault distance is roughly proportional to the increase in fault resistance. However, even with a fault resistance of up to 25 Ω, the protection can still obtain a fault distance result within the action zone $(-1, x_{set})$. Therefore, when internal faults occur on the short-distance line, the protection is capable of withstanding the maximum fault resistance of approximately 25 Ω. In addition, we analyze the error of calculated fault distance under the impact of the fault resistance in detail in [22].

A threshold selection method is designed to avoid possible over-reach under external resistive faults. The above contents are not discussed further in this paper.

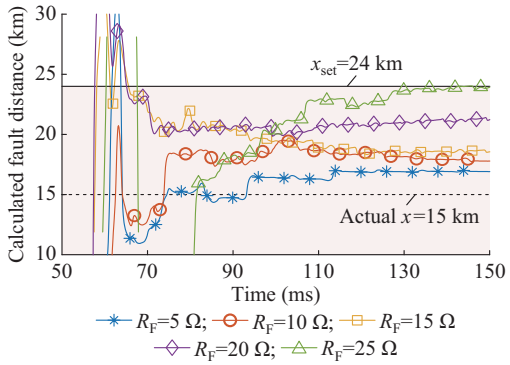

Fig. 13. Calculated fault distances under AG faults at f_2 with various fault resistances.

2) Impact of Noise

It is noteworthy that the weighting method also improves the stability of the proposed algorithm, especially under the impact of noise. For example, an AG fault is set at f_2, and the white Gaussian noises are added to the sampled voltages and currents. The calculated fault distances through the proposed algorithm are shown in Fig. 14, where the signal-to-noise ratios *SNR* are set to be 20 dB and 30 dB. Additionally, the results obtained by the conventional algorithm in (2) are also given for comparison.

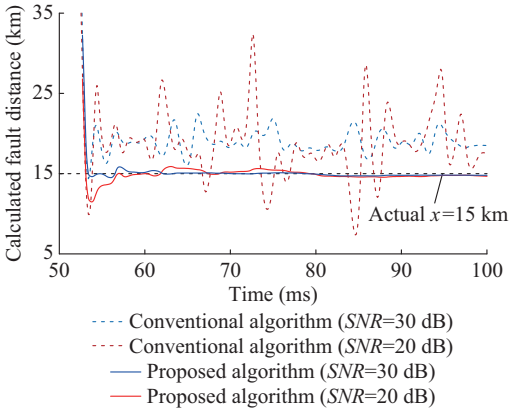

Fig. 14. Calculated fault distances under noise (AG fault at f_2).

Obviously, the calculated fault distance through the conventional algorithm cannot converge under the impact of noise. However, the calculated fault distance through the proposed algorithm converges to the actual fault distance (15 km). This is because the weighting method evaluates the confidence level of each SVD-LSM result by the Euclidean norm, and the unreliable results that are highly affected by noise are weighted down. By continuously weighting, the weighted distance becomes more and more stable and reliable.

3) Impact of Photovoltaic (PV)

The above tests are all performed in the renewable power transmission system based on DFIG, which is the partial-scale inverter-based source. To verify the protection performance under the impact of full-scale inverter-based sources, a detailed model of a PV system is built in RTDS platform, as illustrated in Fig. SA3 in Supplementary Material A. During the fault LVRT, the PV system supplies the positive-se-

quence reactive current and suppresses the negative-sequence current. The corresponding parameters of the PV system are shown in Supplementary Material A Table SAII, and the other parameters of the model are the same as those in Supplementary Material A Table SAI. In addition, considering the suppression strategy for negative-sequence current, the differential equation for phase-to-phase faults is adopted as $u_{M\varphi\varphi}=(R_1 i_{M\varphi\varphi}+L_1 \mathrm{d}i_{M\varphi\varphi}/\mathrm{d}t)x+i_{M\varphi}R'_{\mathrm{F}}$, where the measured current of the faulted phase is used to replace the fault current $i_{\mathrm{F}\varphi\varphi}$.

As shown in Supplementary Material A Fig. SA3, the faults under various conditions are set at f_1-f_6. The experiment is also repeated five times under each fault condition, and the recorded data are shown in Table II. And the typical recorded data of 3-phase fault at f_2 are shown in Supplementary Material A Fig. SA4. According to the test results, even under the impact of PV, the protection can still accurately recognize internal faults at f_1-f_3 and external faults at f_4-f_6, and quickly operate to trip for internal faults within 20 ms.

TABLE II
PROTECTION PERFORMANCE UNDER DIFFERENT CONDITIONS IN PV SYSTEM

Internal/external fault	Fault location	Fault type	x_{m} (km)	t_{op} (ms)
Internal fault	f_1 (0)	AG	−0.1-0.1	14.0-15.7
		AB	0.0-0.2	15.0-16.3
		ABG	0.0-0.2	13.8-15.0
		ABC	0.0-0.3	13.6-14.8
	f_2 (15 km)	AG	14.8-15.1	16.0-18.2
		AB	14.9-15.3	15.5-17.9
		ABG	14.6-15.1	15.2-18.0
		ABC	14.6-15.3	15.3-18.8
	f_3 (23.4 km)	AG	23.2-23.4	15.9-18.7
		AB	23.4-23.7	15.8-18.8
		ABG	23.0-23.5	15.0-19.0
		ABC	23.1-23.9	16.3-19.8
External fault	f_4 (24.6 km)	AG	24.5-24.7	
		AB	24.5-24.9	
		ABG	24.2-24.6	
		ABC	24.3-25.0	
	f_5 (220 kV busbar)	AG	46.4-48.9	
		AB	35.6-36.3	
		ABG	34.6-35.5	
		ABC	35.0-36.2	
	f_6 (backward fault)	AG	−0.1-−0.0	Blocked
		AB	−0.2-−0.0	Blocked
		ABG	−0.2-−0.0	Blocked
		ABC	−0.2-−0.0	Blocked

D. Application in Industrial Power System

According to the relevant standards [26]-[28], the prototype of the protection device successfully passed the third-party testing. The test items include three categories: electrical performance and safety test, electromagnetic compatibility test, and dynamic test. Specifically, the dynamic test is performed on the RTplus platform. In the digital simulation model of RTplus platform, the protected transmission line is connected to a PV system to test the protection performance under the influence of RESs. The detailed dynamic test items include internal and external faults, developing and transferring faults, potential transformer (PT)/current transformer (CT) disconnections, internal/external faults under system frequency deviations, etc. It is verified that the prototype of the protection device can correctly trip within 25 ms under internal faults, while it can reliably remain inactive under external faults and other situations. The above tests prove that the prototype of the protection device meets the requirements of industrial applications.

The prototype of protection device has been applied at the 110 kV Fengtai wind farm and the 35 kV Dashentang wind farm, Tianjin, China, as shown in Fig. 15. The prototype of protection device is used as fast protection for the grid-connected lines, both of which consist of several OHLs or UGCs with inhomogeneous line parameters. Since it is put into trial operation, no faults have occurred, and the prototype of the protection device has never erroneously sent alarm reports or trip signals. Overall, the applied prototype of the protection device can accurately and reliably isolate the internal faults of the renewable power transmission system within 25 ms, even under severe RES transient fault response. On this basis, the delay time of the frequency and voltage protection of the wind farm can be extended, thus avoiding frequent grid disconnection in the case of external faults or any disturbances. Therefore, the prototype of the protection device can greatly improve the power supply reliability and operational stability of the power system with large-scale RESs.

Fig. 15. Prototype of protection device. (a) In 110 kV Fengtai wind farm, Tianjin, China. (b) In 35 kV Dashentang wind farm, Tianjin, China.

V. CONCLUSION

This paper investigates a robust algorithm of time-domain distance protection for renewable power transmission system with mixed lines. According to the mathematical analysis, the inhomogeneity of OHL and UGC not only causes fault location errors, but also generates calculation outliers due to "0/0" problem under weak signals. The SVD-LSM is adopted to solve the differential equations, which eliminates the outliers and improves the reliability of the protection algorithm. Furthermore, a weighting method based on the Euclidean norm is designed to improve computational convergence. Thus, the calculated fault distance is capable of converging to a stable value under 3-phase faults, even by using a short time window. In addition, for the location error

caused by inhomogeneous line parameters, a distance correction method for mixed lines is designed to avoid the protection over- or under-reach.

Based on the proposed algorithm, a prototype of the protection device is developed. Extensive HIL tests verify that the prototype of the protection device can quickly and accurately obtain a convergent fault distance, independent of the inhomogeneous parameters of the mixed line and the transient response of RES. The prototype of the protection device has achieved good operational performance in the actual high-voltage wind power transmission lines. Therefore, the proposed algorithm is a robust, economical, fast, and selective protection solution for power grids with integrated RES.

REFERENCES

[1] M. Haghighat, M. Niroomand, H. D. Tafti *et al*., "A review of state-of-the-art flexible power point tracking algorithms in photovoltaic systems for grid support: classification and application," *Journal of Modern Power Systems and Clean Energy*, vol. 12, No. 1, pp. 1-21, Jan. 2024.

[2] Q. Liu, K. Jia, B. Yang *et al*., "Analytical model of inverter-interfaced renewable energy sources for power system protection," *IEEE Transactions on Power Delivery*, vol. 38, no. 2, pp. 1064-1073, Apr. 2023.

[3] Y. Fang, K. Jia, Z. Yang *et al*., "Impact of inverter-interfaced renewable energy generators on distance protection and an improved scheme," *IEEE Transactions on Industrial Electronics*, vol. 66, no. 9, pp. 7078-7088, Sept. 2019.

[4] U. Uma, D. Nmadu, N. Ugwuanyi *et al*., "Adaptive overcurrent protection scheme coordination in presence of distributed generation using radial basis neural network," *Protection and Control of Modern Power Systems*, vol. 8, no. 1, p. 63, Oct. 2023.

[5] P. Mishra, A. Pradhan, and P. Bajpai, "Adaptive distance relaying for distribution lines connecting inverter-interfaced solar PV plant," *IEEE Transactions on Industrial Electronics*, vol. 68, no. 3, pp. 2300-2309, Mar. 2021.

[6] H. Zhan, C. Wang, Y. Wang *et al*., "Relay protection coordination integrated optimal placement and sizing of distributed generation sources in distribution networks," *IEEE Transactions on Smart Grid*, vol. 7, no. 1, pp. 55-65, Jan. 2016.

[7] H. Zeineldin, H. Sharaf, D. Ibrahim *et al*., "Optimal protection coordination for meshed distribution systems with DG using dual setting directional over-current relays," *IEEE Transactions on Smart Grid*, vol. 6, no. 1, pp. 115-123, Jan. 2015.

[8] B. Li, J. Liu, X. Wang *et al*., "Fault studies and distance protection of transmission lines connected to DFIG-based wind farms," *Applied Sciences*, vol. 8, no. 4, p. 562, Apr. 2018.

[9] A. Hooshyar, M. Azzouz, and E. El-Saadany, "Distance protection of lines connected to induction generator-based wind farms during balanced faults," *IEEE Transactions on Sustainable Energy*, vol. 5, no. 4, pp. 1193-1203, Oct. 2014.

[10] B. Li, Y. Sheng, J. He *et al*., "Improved distance protection for wind farm transmission line based on dynamic frequency estimation," *International Journal of Electrical Power & Energy Systems*, vol. 153, p. 109382, Nov. 2023.

[11] Y. Li, K. Jia, T. Bi *et al*., "Analysis of line current differential protection considering inverter-interfaced renewable energy power plants," in *Proceedings of 2017 IEEE PES Innovative Smart Grid Technologies Conference Europe*, Turin, Italy, Sept. 2017, pp. 1-6.

[12] L. Zheng, K. Jia, T. Bi *et al*., "Cosine similarity based line protection for large-scale wind farms," *IEEE Transactions on Industrial Electronics*, vol. 68, no. 7, pp. 5990-5999, Jul. 2021.

[13] *Technical Specification for Protection Configuration and Setting of Grid-connected Wind Power Plant*, DL/T 1631-2016, China, 2016.

[14] *Technical Specification for Relaying Protection of Photovoltaic Power Station*, GB/T 32900-2016, 2016.

[15] Q. Yang, "Microprocessor based distance protection," Ph. D. dissertation, Department of Electrical Engineering and Computer Science, University of New South Wales, Sydney, Australia, 1981.

[16] M. Wen, D. Chen, and X. Yin, "A novel fast distance relay for long transmission lines," *International Journal of Electrical Power & Energy Systems*, vol. 63, pp. 681-686, Dec. 2014.

[17] X. Chen, X. Yin, and Z. Zhang, "Impacts of DFIG-based wind farm integration on its tie line distance protection and countermeasures," *IEEJ Transactions on Electrical and Electronic Engineering*, vol. 12, no. 4, pp. 553-564, Jul. 2017.

[18] T. Zheng, W. Lv, X. Zhuang *et al*., "Improved time-domain distance protection for asymmetrical faults based on adaptive control of MMC in offshore AC network," *International Journal of Electrical Power & Energy Systems*, vol. 152, p. 109229, Oct. 2023.

[19] Z. Hu, B. Li, Y. Zheng *et al*., "Fast distance protection scheme for wind farm transmission lines considering R-L and bergeron models," *Journal of Modern Power Systems and Clean Energy*, vol. 11, no. 3, pp. 840-852, May 2023.

[20] Y. Zhong, X. Kang, Z. Jiao *et al*., "A novel distance protection algorithm for the phase-ground fault," *IEEE Transactions on Power Delivery*, vol. 29, no. 4, pp. 1718-1725, Aug. 2014.

[21] P. de L. Vianna and G. M. Junior, "Time-domain distance protection of transmission lines based on the conic section general equation," *Electric Power Systems Research*, vol. 205, p. 107740, Apr. 2022.

[22] Z. Xie, B. Li, J. He *et al*., "Error analysis and improved method of time-domain distance protection for wind power transmission lines," *International Journal of Electrical Power & Energy Systems*, vol. 160, p. 110081, Sept. 2024.

[23] D. Tziouvaras and J. Needs, "Protection of mixed overhead and underground cable lines," in *Proceedings of 12th IET International Conference on Developments in Power System Protection*, Copenhagen, Denmark, Mar. 2014, pp. 1-6.

[24] J. Han, "Fault location on mixed overhead line and cable network," Ph. D. dissertation, School of Electrical and Electronic Engineering, The University of Manchester, Manchester, the United Kingdom, 2015.

[25] A. Zahran, N. Elkalashy, M. Elsadd *et al*., "Improved ground distance protection for cascaded overhead-submarine cable transmission system," in *Proceedings of 2017 Nineteenth International Middle East Power Systems Conference*, Cairo, Egypt, Dec. 2017, pp. 758-778.

[26] *Basic Testing Method for Relaying Protection and Security Automatic Equipment*, GB/T 7261-2016, 2016.

[27] *Measuring Relays and Protection Equipment – Part 1: Common Requirements*, GB/T 14598.2-2011, 2011.

[28] *Dynamic Test of Power System Protective Products*, GB/T 26864-2011, 2011.

Bin Li received the B.Sc., M.Sc., and Ph.D. degrees in electrical engineering from Tianjin University, Tianjin, China, in 1999, 2002, and 2005, respectively. Currently, he is a Professor of the Key Laboratory of Smart Grid of Ministry of Education, Tianjin University. His research interests include the protection and control of power system.

Zhongrun Xie received the B.Sc. and M.Sc. degrees in electrical engineering from Shandong University, Jinan, China, in 2017 and 2020, respectively. Currently, he is pursuing the Ph.D. degree in the Key Laboratory of Smart Grid of Ministry of Education, Tianjin University, Tianjin, China. His research interests include fault analysis and protection of power system.

Jiawei He received the B.Sc., M.Sc., and Ph.D. degrees in electrical engineering from Tianjin University, Tianjin, China, in 2014, 2017, and 2021, respectively. Now he is an Associate Researcher Fellow in the Key Laboratory of Smart Grid of Ministry of Education, Tianjin University. His research interests include protection and control of power system.

Mingyu Shao received the B.Sc. degree in electrical engineering from Tianjin University, Tianjin, China, in 2023. Currently, he is pursuing the M.Sc. degree in the Key Laboratory of Smart Grid of Ministry of Education, Tianjin University, Tianjin, China. His research interests include protection and control of power system.

Haiji Wang received the M.Sc. degree in electrical engineering from Tianjin University, Tianjin, China, in 2002. Currently, he is the Chief Engineer of Xi'an XIRUI Control Technology Co., Ltd., Xi'an, China. His research interests include research and development of power system protection and control device.

Zepeng Hu received the B. Sc. degree in electrical engineering from Chongqing University, Chongqing, China, in 2019. Currently, he is pursuing the M.Sc. degree in the Key Laboratory of Smart Grid of Ministry of Education, Tianjin University, Tianjin, China. His research interests include protection and control of power system.